Check for updates

Time resolved Fabry-Perot measurements of cavity temperature in pulsed QCLs

S. GUNDOGDU,[1] H. S. PISHEH,[1] A. DEMIR,[1] M. GUNOVEN,[2] A. AYDINLI,[3] AND C. SIRTORI[4]

[1]*Physics Department, Bilkent University, Ankara, 06800, Turkey*
[2]*Physics Department, Middle East Technical University, Ankara, 06800, Turkey*
[3]*Currently Electrical and Electronics Engineering Department, Uludağ University, Bursa, 16059 Turkey*
[4]*Laboratoire Materiauxet Phenomenes Quantiques, Univ. Paris Diderot, Paris 7, France*

Abstract: Temperature rise during operation is a central concern of semiconductor lasers and especially difficult to measure during a pulsed operation. We present a technique for in situ time-resolved temperature measurement of quantum cascade lasers operating in a pulsed mode at ~9.25 μm emission wavelength. Using a step-scan approach with 5 ns resolution, we measure the temporal evolution of the spectral density, observing longitudinal Fabry-Perot modes that correspond to different transverse modes. Considering the multiple thin layers that make up the active layer and the associated Kapitza resistance, thermal properties of QCLs are significantly different than bulk-like laser diodes where this approach was successfully used. Compounded by the lattice expansion and refractive index changes due to time-dependent temperature rise, Fabry-Perot modes were observed and analyzed from the time-resolved emission spectra of quantum cascade lasers to deduce the cavity temperature. Temperature rise of a QCL in a pulsed mode operation between −160 °C to −80 °C was measured as a function of time. Using the temporal temperature variations, a thermal model was constructed that led to the extraction of cavity thermal conductivity in agreement with previous results. Critical in maximizing pulsed output power, the effect of the duty cycle on the evolution of laser heating was studied in situ, leading to a heat map to guide the operation of pulsed lasers.

OCIS codes: (250.0250) Optoelectronics; (140.5965) Semiconductor lasers, quantum cascade.

References and links

1. J. Faist, F. Capasso, D. L. Sivco, C. Sirtori, A. L. Hutchinson, and A. Y. Cho, "Quantum cascade laser," Science **264**(5158), 553–556 (1994).
2. Q. J. Wang, C. Pflügl, L. Diehl, F. Capasso, T. Edamura, S. Furuta, Y. Masamichi, and H. Kan, "High performance quantum cascade lasers based on three-phonon-resonance design," Appl. Phys. Lett. **94**(1), 011103 (2009).
3. Y. Bai, N. Bandyopadhyay, S. Tsao, S. Slivken, and M. Razeghi, "Room temperature quantum cascade lasers with 27% wall plug efficiency Room temperature quantum cascade lasers with 27% wall plug efficiency," Appl. Phys. Lett. **98**(18), 181102 (2011).
4. M. Razeghi, S. Slivken, Y. Bai, B. Gokden, and S. R. Darvish, "High power quantum cascade lasers," New J. Phys. **11**(12), 125017 (2009).
5. A. Lyakh, R. Maulini, A. Tsekoun, R. Go, C. K. Patel, and N. Patel, "Multiwatt long wavelength quantum cascade lasers based on high strain composition with 70% injection efficiency," Opt. Express **20**(22), 24272–24279 (2012).
6. M. S. Vitiello, G. Scalari, B. Williams, and P. De Natale, "Quantum cascade lasers: 20 years of challenges," Opt. Express **23**(4), 5167–5182 (2015).
7. M. A. Belkin and F. Capasso, "New frontiers in quantum cascade lasers: high performance room temperature terahertz sources," Phys. Scr. **90**(11), 118002 (2015).
8. V. Spagnolo, M. S. Vitiello, C. D. I. Franco, and G. Scamarcio, "Thermal Modelling of Quantum Cascade Lasers," in Proceedings of the International School and Conference on Photonics, **116**(4) (2009).
9. M. S. Vitiello and G. Scamarcio, "Anisotropic heat propagation velocity in quantum cascade lasers," Appl. Phys. Lett. **96**(10), 101101 (2010).

10. M. Süess, R. Peretti, Y. Liang, J. Wolf, C. Bonzon, B. Hinkov, and J. Faist, "Advanced Fabrication of Single-Mode and Multi-Wavelength MIR-QCLs," Photonics **3**(2), 26 (2016).
11. M. Razeghi, J. S. Yu, A. Evans, S. Slivken, S. R. Darvish, J. E. David, J. Nguyen, B. Gokden, and S. Khosravani, "Quantum cascade laser progress and outlook," in Optically Based Biological and Chemical Sensing for Defence, vol. 5617, (International Society for Optics and Photonics, 2004.),pp. 221–233.
12. T. Alexei, R. Go, M. Pushkarsky, M. Razeghi, C. Kumar, and N. Patel, "Improved performance of quantum cascade lasers through a scalable, manufacturable epitaxial-side-down mounting process," in Proceedings of the 103, no. 13 (National Academy of Sciences of the United States of America, 2006),pp. 4831–4835.
13. K. Pierściński, D. Pierścińska, M. Iwińska, K. Kosiel, A. Szerling, P. Karbownik, and M. Bugajski, "Investigation of thermal properties of mid-infrared AlGaAs/GaAs quantum cascade lasers," J. Appl. Phys. **112**(4), 043112 (2012).
14. D. Pierścińska, K. Pierściński, M. Płuska, Ł. Marona, P. Wiśniewski, P. Perlin, and M. Bugajski, "Examination of thermal properties and degradation of InGaN - based diode lasers by thermoreflectance spectroscopy and focused ion beam etching," AIP Adv. **7**(7), 075107 (2017).
15. D. Pierścińska, A. Kozlowska, K. Pierściński, M. Bugajski, J. W. Tomm, M. Ziegler, and F. Weik, "Thermal processes in high-power laser bars investigated by spatially resolved thermoreflectance," J. Mater. Sci. Mater. Electron. **19**(S1), 150–154 (2008).
16. D. Pierścińska, Ł. Marona, K. Pierściński, P. Wiśniewski, P. Perlin, and M. Bugajski, "High-resolution mirror temperature mapping in GaN-based diode lasers by thermoreflectance spectroscopy," Jpn. J. Appl. Phys. **56**(2), 020302 (2017).
17. D. Pierścińska, K. Pierściński, M. Morawiec, P. Karbownik, P. Gutowski, and M. Bugajski, "CCD thermoreflectance spectroscopy as a tool for thermal characterization of quantum cascade lasers," Semicond. Sci. Technol. **31**(11), 115006 (2016).
18. S. Fathololoumi, D. Ban, H. Luo, E. Dupont, S. R. Laframboise, A. Boucherif, and H. C. Liu, "Thermal behavior investigation of terahertz quantum-cascade lasers," IEEE J. Quantum Electron. **44**(12), 1139–1144 (2008).
19. V. Spagnolo, G. Scamarcio, D. Marano, M. Troccoli, F. Capasso, C. Gmachl, A. M. Sergent, A. L. Hutchinson, D. L. Sivco, A. Y. Cho, H. Page, C. Becker, and C. Sirtori, "Thermal characteristics of quantum-cascade lasers by micro-probe optical spectroscopy," IEE Proc., Optoelectron. **150**(4), 298–305 (2003).
20. C. Pflügl, M. Litzenberger, W. Schrenk, D. Pogany, E. Gornik, and G. Strasser, "Interferometric study of thermal dynamics in GaAs-based quantum-cascade lasers," Appl. Phys. Lett. **82**(11), 1664–1666 (2003).
21. T. L. Paoli, "A New Technique for Measuring the Thermal Impedance of Junction Lasers," IEEE J. Quantum Electron. **11**(7), 498–503 (1975).
22. J. S. Manning, "Thermal impedance of diode lasers: Comparison of experimental methods and a theoretical model," J. Appl. Phys. **52**(5), 3179–3184 (1981).
23. B. S. Bhumbra, G. H. B. Thompson, and A. P. Wright, "Thermal impedance measurement of semiconductor lasers," Electron. Lett. **30**(10), 793–794 (1994).
24. E. Duda, J. C. Carballes, and J. Apruzzese, "Thermal resistance and temperature distribution in double-heterostructure lasers: Calculations and experimental results," IEEE J. Quantum Electron. **15**(8), 812–817 (1979).
25. M. Bertolotti, V. Bogdanov, A. Ferrari, A. Jascow, N. Nazorova, A. Pikhtin, and L. Schirone, "Temperature dependence of the refractive index in semiconductors," J. Opt. Soc. Am. B **7**(6), 918 (1990).
26. M. Brandstetter, A. Genner, C. Schwarzer, E. Mujagic, G. Strasser, and B. Lendl, "Time-resolved spectral characterization of ring cavity surface emitting and ridge-type distributed feedback quantum cascade lasers by step-scan FT-IR spectroscopy," Opt. Express **22**(3), 2656–2664 (2014).
27. B. Hinkova, Q. Yang, F. Fuchs, B. Bronner, K. Köhler, and J. Wagner, "Time-resolved characterization of external-cavity quantum-cascade lasers," Appl. Phys. Lett. **94**(22), 221105 (2009).
28. J. Melkonian, J. Petit, M. Raybaut, A. Godard, and M. Lefebvre, "Time-resolved spectral characterization of a pulsed external-cavity quantum cascade laser," in Conference on Lasers and Electro-Optics 2012, OSA Technical Digest (online) (Optical Society of America, 2012), paper CF2K.4.
29. N. N. Sirota, V. V. Novikov, and A. M. Antiukhov, Dokl. Akad. Nauk SSSR **263**(1), 96–100 (1982).
30. U. Z. Piesbergen, Naturforschung**18a**, 2 141–147 (1963).
31. V. Palankovski, "Simulation of Heterojunction Bipolar Transistors," Dissertation, Technische Universität Wien, 2000. http://www.iue.tuwien.ac.at/phd/palankovski.
32. A. Lops, V. Spagnolo, and G. Scamarcio, "Thermal modeling of GaInAs/AlInAs quantum cascade lasers," J. Appl. Phys. **100**(4), 043109 (2006).

1. Introduction

Quantum cascade lasers are coherent light sources that rely on intersubband transitions of multilayer semiconductor quantum well structures and can be designed to emit light from short wave infrared to terahertz frequencies. They were first demonstrated in 1994 at Bell Laboratories [1] and since then, intensive research has been done to achieve watt level optical output powers at room temperature [2–5] for mid and long wave IR wavelengths. For

terahertz QCL, it is still a challenge to achieve both room temperature and high-power operation [6-7].

Operation of QCLs strongly depend on temperature, both in terms of threshold current density and wall plug efficiency. Although QCLs with up to 27% wall-plug-efficiency at room temperature has been demonstrated [3], they still generate a lot of heat, therefore, thermal management of QCLs has a significant contribution to device performance. The thermal conductivity of the active region of the QCL is anisotropic and significantly less than the corresponding bulk material due to a high number of interfaces resulting in increased diffuse phonon scattering and Kapitza resistance [8-9] which makes it even more complicated to optimize thermal properties. To increase thermal conduction, however costly, it is common to regrow insulating epitaxial material to refill the trenches that form the waveguide [3-4,10] increasing the lateral heat transfer. Other common thermal management methods are electroplating thick gold layer on top of the laser waveguide and mounting the QCL epi-side down on high thermal conductivity submounts such as AlN, sapphire or diamond [11-12]. To evaluate the effect of these methods on thermal performance, one should measure the temperature of the laser in situ.

Methods for measurements of temperature and other thermal properties of semiconductor lasers include thermoreflectance (TR) [13–17], time-resolved microprobe photoluminescence (PL) [9,18-19], scanning interferometric thermal mapping technique (SITM) [20] and techniques that use frequency shift of Fabry-Perot (FP) modes [21–24]. The first two methods use a laser source to measure light reflection intensity or photoluminescence spectrum to measure surface temperature. For the TR method, the surface reflectivity and for the PL method, the peak wavelength of photoluminescence is calibrated against a steady state heat sink temperature, enabling the measurement of the temperature during the operation of the laser. These techniques measure surface temperatures and typically are used on the laser facets. However, depending on the laser and its fabrication process, packaging and operating conditions, thermal properties on the facet surface and hence facet temperatures may differ from the bulk of the optical cavity. Since performance of a typical QCL crystal is strongly affected by temperature, time-resolved cavity temperature during operation is a valuable information for laser characterization. SITM is a technique that can measure the temperature within the cavity using a scanning laser probe to map photoluminescence peak wavelength. Excitation laser is focused from the transparent substrate side; therefore, it can directly measure the PL signal from the cavity, which is correlated with temperature. Measurement of the wavelength shift of FP modes is a widespread and easy technique for analysis of thermal impedance of diode lasers [21–24]. In this method, either frequency shift is measured as a function of temperature or duty cycle of the laser is varied while adjusting the heat sink temperature to keep the emission frequency constant. These methods are used to deduce the thermal resistance from the active region to the heat sink. For diode lasers, a typical value for the temperature induced FP shift is of the order of 0.1 nm/°C [22]. Unlike the bulk-like-structure of most laser diodes, QCLs with extremely thin multiple layers in their active region presents an anisotropic and low thermal conductivity that governs the temperature dynamics. Due to emission in the mid infrared, step-scan time resolved FTIR spectroscopy can be used to observe Fabry-Perot modes of QCLs. Step-scan approach was previously used to study tuning and mode hopping behavior of DFB and ring QCLs [26] as well as to measure time delay between external and internal modes of external cavity QCL [27] and sum frequency mixing of nanosecond pulses was used to study QCL mode dynamics [28]; however, use of FP modes to deduce temperature in QCLs is lacking.

In contrast with previous work on temperature dynamics of QCLs using TR, PL and SITM, in this work, we used FP modes in the time-resolved emission spectrum of a pulsed QCL to measure time-dependent temperature using a FTIR spectrometer in step-scan mode. This method has the advantage of measuring the temperature directly within the cavity, and is relatively simple since it does not require an external optical setup and a scanning probe

mechanism. FP modes appear as periodic fluctuations in the emission spectrum due to reflection between two laser facets. One can extract two separate pieces of information from FP modes; first one is the peak frequencies of these periodic features; $m/2dn_g$, where d is the cavity length, n_g is the group refractive index, and m is an integer. The second is the period of FP mode frequencies which is $\Delta f = 1/2dn_g$. They both depend on the refractive index, and the cavity length, yet differ from each other by the factor m, which is of the order of 10^3 in our case. Therefore, frequencies of FP peaks are much more sensitive to the variations in the refractive index and cavity length compared to the period of FP modes. Thermal expansion coefficients of semiconductors are typically of the order of 10^{-6} K^{-1}, which corresponds to a mechanical extension of 1nm/K for a 1mm cavity, and temperature derivative of refractive index is of the order of 10^{-4} K^{-1} [25], and therefore the contribution of refractive index change dominates.

2. Experimental

QCL epicrystals were grown by a commercial facility. The active region design is a 3-phonon resonant scheme similar to the design presented by Wang et al. [2]. In this scheme, the energy difference between four lower consecutive quantum well states is equal to the LO phonon energy of the crystal, so that an electron decayed into the low energy state quickly empties that state by following phonon scattering three times, facilitating population inversion and - reducing thermal back-filling of the lower laser level by the electrons from the active region ground state. The design consists of an active region of lattice matched InGaAs/AlInAs quantum wells of 40 periods with a total thickness of 2.7 μm. The overall structure is: 100nm InGaAs(5E18) / 850nm InP(5E18) / 2500nm InP(5E16) / 200nm InGaAs (5E18) / Active region / 200nm InGaAs(5E18) / 2000nm InP(5E16) / 50nm InGaAs(1E18)/ Buffer InP (5E18)/Substrate InP(5E18). Si doping levels are shown in the parentheses. A waveguide was formed by wet etching of two 20μm-wide trenches. 400 nm PECVD grown silicon nitride was used as an insulating layer and contact windows on top of the waveguides was formed by HF etching. 20nm Ti and 100nm Au for top contact and GeAu/Ni/Au (40/40/150 nm) for bottom contact were evaporated by e-beam. Top contact was electroplated with 5μm thick gold. Facets were cleaved with a diamond scriber and 2mm-long cavities were formed. Epi-side up chips were mounted on Au-plated copper holders and top contacts were wire bonded on Au-plated PCB pads.

Time-resolved spectral measurements (TRS) were done using Bruker Vertex 70V FTIR spectrometer in step-scan mode. This mode records time-resolved photodetector signal when the interferometer stops at predetermined interferogram steps and repeats the procedure for many steps, enabling high-resolution time-resolved spectra. A liquid nitrogen cooled fast MCT detector was used to achieve a time resolution of 5ns. Spectral resolution of the setup was 0.5cm^{-1}. Samples were mounted in a LN-cooled dewar with a ZnSe window. Voltage pulsers were used as a trigger source for FTIR step scan measurements. Two different voltage pulsers were used; the first one was used to apply voltage pulses of 2.0 μs with an amplitude between 14 and 19V with a typical rise time of 250ns, the second one was used to apply 5.0 μs pulses but with a 140ns rise time with a fixed voltage of 18V.

3. Results and discussion

A typical time-resolved spectrum of the QCL excited with 2μs pulsewidth is shown in Fig. 1a. The temporal scale starts with the initiation of voltage pulser. A single lateral mode is initiated with a peak around 1084 cm^{-1} at 250 ns after the pulser is turned on. At 500 ns, a second mode develops with FP modes overriding them. Features with approximately 40cm^{-1} width are due to lateral FP modes of the cavity and features with ~0.7cm^{-1} width are due to longitudinal FP modes. The mode hopping behavior between the lateral modes may be due to

both changes in the cavity temperature and instability of the voltage at the beginning of the pulse. However, the shift in the longitudinal FP modes with time does not show hopping behavior, which makes them easy to process further. Figure 1(b) summarizes the time-resolved spectra in a heat map. After the onset of lasing with two lateral modes, we observe well established longitudinal FP modes that last for the duration of the voltage pulse while shifting with time.
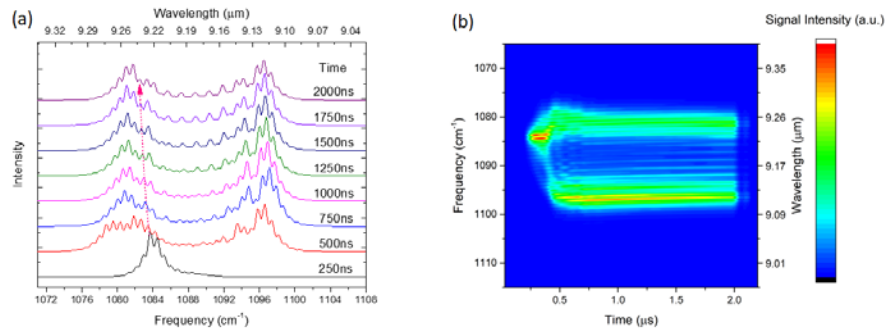

Fig. 1. A time resolved spectra of a QCL operating in pulsed mode, spectra is shifted for clarity a). Cavity length is 2mm and waveguide width is 12μm. Voltage pulse has an amplitude of 17.03V with 2μs duration. Heat map of the time resolved spectral data, b).

Since these two features have different spectral widths, it is easy to separate them using a fast Fourier transform (FFT) highpass, Fig. 2(a) and a lowpass filter, Fig. 2(b), where high pass filter reveals fine structure of the longitudinal FP modes and low pass filter displays the lateral FP mode envelopes. Lateral FP mode peaks shift toward the longer wavelengths, as the laser heats up.
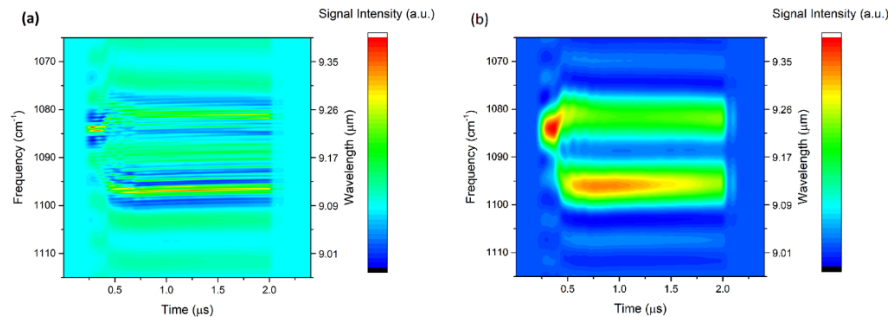

Fig. 2. Time resolved spectrum of the QCL after highpass, a) and lowpass filtering, b).

To examine temperature dependence of the lateral FP shifts, we controlled the sink temperature of the laser using a PID controlled heater and a temperature sensor. At various heat sink temperatures, we measured the spectrum at 140ns after the initiation of the 5 μs pulse, before the pulse has time to heat the sample. Voltage pulse duty cycle was 1% to allow the laser to reach the sink temperature between the pulses. Cavity temperature was assumed to be at the heat sink temperature at the beginning of each pulse. We measured the frequency shifts of the spectra as a function of heat sink temperature from the FFT of the spectra. To calculate the frequency shifts in a standardized way, we calculated the peak in the FFT amplitude that corresponds to the $1/\Delta f$, where Δf is the frequency difference between two FP peaks, and recorded the FFT phase constant, φ, at the corresponding value. In our case, the peak of the FFT amplitude is at 1.29 cm, and $\Delta f = 0.78$ cm^{-1}. Then, frequency shifts in cm^{-1} unit were calculated from $\Delta f * \varphi / \pi$. It should be noted that the phase of the FFT signal has a $\varphi = 0$ reference point that depends on how the spectrum is sampled. For this reason, all data

should be sampled within the same frequency range and sampling interval. The data is shown in Fig. 3(a). The FP modes, as well as their red shift, is clearly observed. Compiling the time-dependent FP shift data, we find a linear relationship in this temperature regime, Fig. 3(b). The FFT amplitude of a spectrum is shown in Fig. 3(b) inset; the peak due to FP modes is indicated by the red arrow.
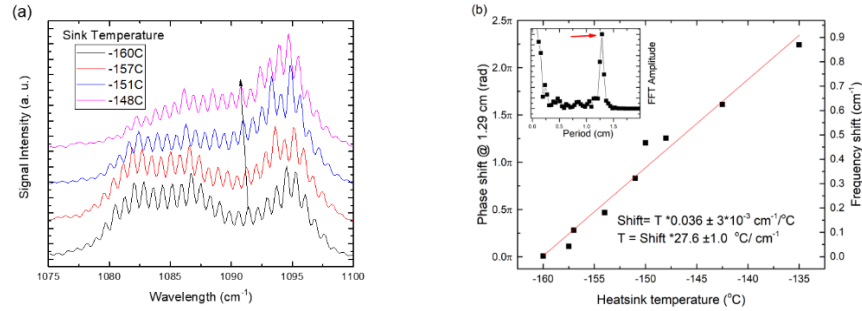

Fig. 3. (a) Emission spectra at varied sink temperatures at 500 ns after the pulse starts. Pulse width is 5µs and duty cycle is 1%. (b) Phase and frequency shifts of the FP modes as a function of sink temperature. Inset shows FFT amplitude of the spectrum at −160°C.

Using temperature dependence of the phase shift, and the FP shift versus time data we obtained time resolved cavity temperatures, Fig. 4(a). These measurements were done at 1% duty cycle for laser to cool down to the heat sink temperature at the end of each pulse and the pulse width was 5 µs. Temperature rise for various heat sink temperatures under constant pulse conditions have been measured. Above a certain temperature, laser emission ceases and above that point measurement cannot be done. In Fig. 4(b), the temporal dependence of temperature rise as a function of pulsed bias power is shown. As expected, the temperature rise increases as a function of pulsed pump power. For different input powers and FP phases, temperatures are equal at the onset of lasing. This indicates that the heating is minimal during the rise time of the voltage pulse due to the high impedance of the laser at lower voltages.

To estimate the effective thermal conductivity of the active region, and to gain more insight into the relationship between maximum and average temperatures, we modeled the laser structure using Comsol Multiphysics wave optics and heat transport modules. Waveguide with 12 µm width was defined with two semi-circular trenches with 6.4 µm depth similar to our fabrication geometry. Specific heat and thermal conductivity of InP and InGaAs layers outside the active region were defined using their bulk values as a function of temperature. For specific heat, an empirical formula, $c_V(T) = C_0 \left(1 - e^{-k_t T}\right)$ was used to fit the experimental data from [29–31], and for thermal conductivity, $\kappa(T) = \kappa_{300}(T/300K)^{\alpha}$ from [31] was used. For the specific heat of the active region, C_0 and k_t values were calculated from a weighted average of InGaAs and AlInAs. Values for C_0, k_t, κ_{300} and α are shown in Table 1.

Table 1. Fit parameters for functions of thermal properties used in simulations.

Material	K_{300} (W/m.K)	A	C_0 (J/gK)	$k_t\left(1/K\right)$
InP	68 [29]	−1.4 [29]	0.373 [28]	6.42*10⁻³ [28]
InGaAs	4.8 [29]	−1.175 [29]	0.318 [27]	8.00*10⁻³ [27]
Active region	-	-	0.344	7.54*10⁻³

The thermal conductivity of the active region k_{act} was defined as a fitting parameter and was initially assumed to be isotropic and constant in temperature. Electrical input power was defined as a heat source dissipated homogeneously on the active region. Eigenmodes were

calculated to find optical mode profiles, and heat transfer equation was solved to calculate time-dependent temperatures. Finally, lowest order TM mode electric field $E(x, y)$ was used to calculate the average temperature as;

$$T_{avg}(t) = \int E(x,y)^2 T(x,y,t)\, dxdy \,/ \int E(x,y)^2 \, dxdy.$$

Here, we assumed that the average temporal temperature follows mainly the spatial distribution of the local optical field intensity, which grows with increasing current, and thus dissipated power. Experimental data in Fig. 4.b was used as a reference and k_{act} value was varied to fit the reference and $T_{avg}(t)$. To fit the calculated temperatures to the experimental data an objective function was defined as; $f = \sum_P \int T_{meas}(t,P) - T_{avg}(t,P)\, dt. T_{meas}(t,P)$ is the experimentally measured temperatures as a function of time at electrical input power, P. Variational minimization of the objective function was carried out for k_{act}. Best fit was obtained for $k_{act} = 2.1 \mp 0.1$ W/m.K. This value is comparable to the thermal conductivity values obtained for QCLs with InGaAs/AlInAs epitaxial structures reported in the literature [9,32]. We also examined the effect of anisotropy of k_act on the measured temperatures by varying the in plane (k_x) and out of plane (k_y) thermal conductivities. We calculated the variation of temperature at the end of the pulse with respect to k_x and k_y, which are,

$$dT_{avg}(t = 2\mu s, k_y = 2.1) / dk_x = -0.06 \mathrm{K} / (\mathrm{W} / (\mathrm{m.K})),$$

$$dT_{avg}(t = 2\mu s, k_x = 2.1) / dk_y - 27.2 \mathrm{K} / (\mathrm{W} / (\mathrm{m.K})).$$

These are order of magnitude values for typical input powers in these types of structures as noted in the inset of Fig. 4b. Average temperatures show very low dependency to the in-plane thermal conductivities compared to out of plane. This is due to thin geometry of the active region and majority of the heat flowing towards the substrate. These results are consistent with previous work using a different approach [32]. Therefore, k_{act} calculated here is close to actual out-of-plane conductivity, and we expect the in-plane conductivity to be higher. To examine the effect of boundaries, we replaced the gold layer with InP and calculated $dT_{avg} / dk_x = -0.09 \mathrm{K} / (\mathrm{W} / (\mathrm{m.K}))$ and $dT_{avg} / dk_y = -15.4$ K $/ (\mathrm{W} / (\mathrm{m.K}))$. They still differ by two orders of magnitude.
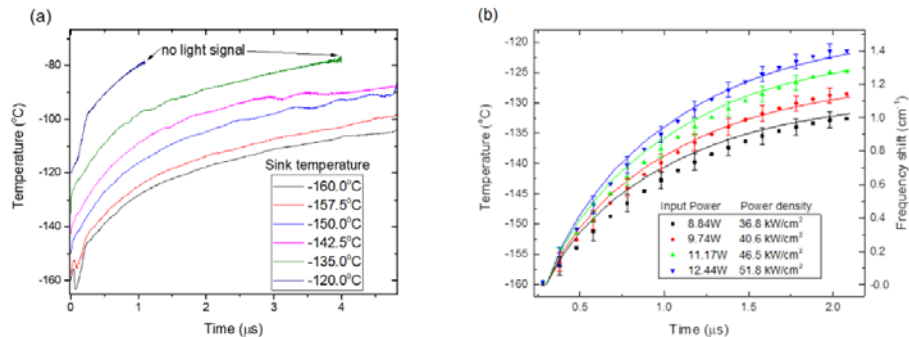

Fig. 4. Measured cavity temperatures with respect to time for varied sink temperatures at constant electrical input power, a) and temperature rise as a function of time for various input powers. Measured temperatures are indicated with symbols and simulated temperatures are indicated with solid lines. Estimated errors are also shown.b).

In Fig. 5(a) we show the square of the electric field of the calculated fundamental TM mode of the QCL, (b) temperature distribution when initial temperature is $T_0 = -160^o C$, input power = 8.2W, 2mm-long 12μm-wide laser at t = 2μs after the pulse starts. Due to the high contrast between thermal conductivities of the active region and surrounding material, temperature rise seems to be confined to the active region and cladding temperatures are close to the sink temperature. This large gradient of temperature distribution causes a difference between the calculated average temperature (−114°C, in the case shown), and the maximum temperature (−131°C) in the active region.
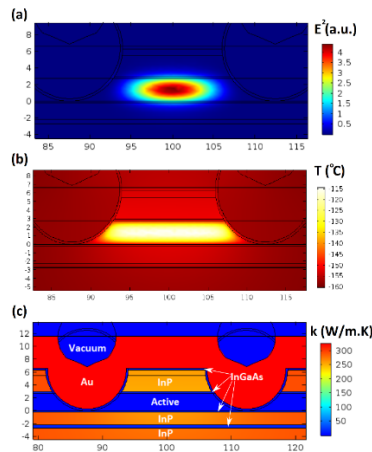
Fig. 5. Square of the calculated optical mode electric field profile, $E^2(x, y)$, a), temperature distribution at t = 2μs, b) and thermal conductivities at t = 2μs c).

Optical power is always a sought-after quantity and beyond the opportunities offered by design and fabrication processes, increasing the input power is the only option. In QCLs, under pulsed operation conditions, input power is limited by a relatively narrow range of voltages applicable. Duty cycle is typically the only free operational parameter which can be increased. Knowing the effects of duty cycle on the thermal performance of the laser may be critical in a lot of cases. We, therefore, measured the effect of duty cycle on time-dependent temperature rise for fixed 5 μs pulse widths, Fig. 6.
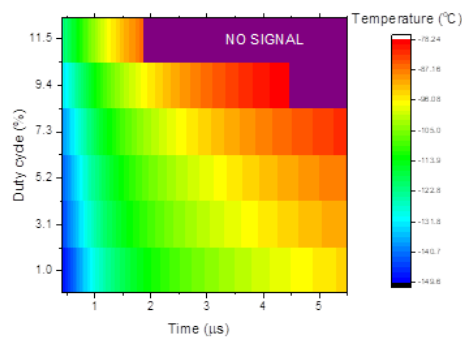
Fig. 6. Measured temperatures as a function of time from the starting of the pulse, and the duty cycle of the pulse. Above −80C, laser does not lase.

At increased duty cycles, the temperature rise is faster compared to lower duty cycles at the same temperature, due to accumulating heat in the substrate at the vicinity of the cavity.

This laser appears to stop lasing slightly above ~-80C, and above that, it is not possible to measure the temperature. This threshold temperature is also consistent between measurements. Construction of a heat map like this one for a QCL provides a convenient tool for the user allowing the choice of operating conditions for a given temperature rise.

This technique has a few caveats, however: first, a temperature can only be measured during lasing and second, a known reference temperature, such as the sink temperature, is needed and continuous measurements are required starting from the reference heat sink temperature so that the phase shifts between successive measurements is less than 360 degrees. Voltage pulses should also be stable since the waveguide index, therefore, FP shifts also depend on the associated electric field. A lot of voltage pulsers tend to have spurious high-frequency oscillations due to the mismatch between the pulser output impedance and the load impedance including the connecting wires at the start and the end of the pulse, particularly when the conductor wires to the laser are long. This causes fluctuations in the measured data as in Fig. 4a. Also, if rise time of the pulse is long, there will be a region in which laser heats due to current before the measurement can be started, depending on the current-voltage characteristics and threshold current of the laser as well. Absolute temperatures may differ a few degrees depending on the difference between the measured heat sink temperature and off-state laser temperature, yet, relative temperatures at each pulse have a resolution better than 0.2 °C. Broad emission spectra that contain many FP periods lead to high temperature measurement resolution. This enables to measure phase shifts less than the resolution of the spectrometer.

QCLs, in general, are highly temperature dependent devices and characterization of thermal properties are crucial for optimization of the performance. Despite complex properties we demonstrated the possibility of using Fabry Perot modes to determine in situ temperature rise in QCLs during pulsed operation. We used time-resolved FP mode spectrum of a QCL to measure in situ temperatures, the thermal conductivity of the active region. This method is a relatively simple and convenient tool for in situ measurement of these properties.